RSC Advances

PAPER

View Article Online
View Journal | View Issue

Cite this: *RSC Adv.*, 2017, **7**, 13159

Controlling structural and magnetic properties of IONPs by aqueous synthesis for improved hyperthermia†

Debora Bonvin,[a] Alla Arakcheeva,‡[b] Angel Millán,[c] Rafael Piñol,[c] Heinrich Hofmann[a] and Marijana Mionić Ebersold*[ade]

Received 16th January 2017
Accepted 16th February 2017

DOI: 10.1039/c7ra00687j

rsc.li/rsc-advances

Iron oxide nanoparticles (IONPs) were synthesized by a novel aqueous synthesis route which combines co-precipitation (CP) and hydrothermal (HT) treatment, termed CP + HT, and compared with IONPs obtained by the standard CP method. Properties of both types of IONPs, including their morphology, diameters, composition, structure and crystallinity, as well as magnetic properties and toxicity were studied and correlated with the synthesis route. Their potential application as mediators for hyperthermia treatment has been evaluated by the specific absorption rate (SAR). Studies showed that IONPs obtained by a novel CP + HT route have a more controlled morphology, structure and crystallinity, leading to better magnetic properties and SAR as compared to IONPs synthesized by CP. Reported IONPs are also not toxic as shown by two assays in two cell lines. These results suggest that our IONPs are suitable for biomedical applications, especially as mediators for the hyperthermia treatment.

Introduction

Magnetic nanoparticles (MNPs) are widely used for numerous applications from solid state[1] to biomedical ones.[2–4] MNPs also have a large, unexploited potential for diagnostics, especially as MRI contrast agents, and for therapy, for instance *via* magnetically-induced hyperthermia.[5] These possibilities are currently driving many research goals.[6–11] Some of the most studied MNPs are iron oxide nanoparticles (IONPs), because of their biocompatibility, metabolization in the body, and versatile synthesis and properties.[12] Magnetite (Fe_3O_4) has larger values for all desirable magnetic properties than maghemite (γ-Fe_2O_3); however the latter is preferred for biomedicine because the presence of Fe^{2+} in the former promotes oxidative stress.[13] Moreover, superparamagnetic IONPs are favoured over ferromagnetic ones, since the latter fosters thrombosis and agglomeration.[14]

One of the promising minimally-invasive cancer treatments is magnetically-mediated hyperthermia based on the sensitivity of cancer cells to temperatures ~41 °C (ref. 15 and 16) generated by MNPs, located in tumour tissues, all placed in a homogeneous alternating magnetic field with frequency f and amplitude H.[17,18] Due to both the maximal energy to which humans can be exposed and to temperature fluctuations, there is a limit for the product $f \cdot H$, which is for the smaller exposed volume (like in a coil of 10 cm in diameter) $\sim 5 \times 10^9$ A m^{-1} s^{-1}.[19,20] The heat generated by MNPs induces either directly cell death or tissue sensitization to increase the efficacy of other anti-cancer therapies. The heating ability of MNPs is quantified by the rate of heat dissipation per unit mass of MNPs; this is termed the specific absorption rate (SAR). Currently, one of the main obstacle for clinical applications of hyperthermia is that successful hyperthermia treatment requires large amounts of IONPs injected directly to the targeted site, as employed by Magforce.[21] This excludes systemic injection, which would for example be essential for treating inaccessible metastases. Thus, there is a need to develop MNPs which have both higher SAR values for improved treatment with reduced injected dose, and which are effective under the clinically allowed $f \cdot H$ conditions.

Besides f and H, SAR is also a complicated non-linear function of the anisotropy constant K, the magnetic volume V_m, and the saturation magnetization M_s, where optimization of the first two variables has the largest effect on increasing SAR.[22,23] The anisotropy constant has different contributions, among which the shape anisotropy has been mostly used for K increase in MNPs. Typically, the magnetic volume is smaller than the MNPs' volume due to structurally disordered in the "bulk" of a MNP and/or at the surface layer having disordered spins. Besides this, the optimal magnetic volume for SAR maximization in ideal spherical IONPs

[a]*Powder Technology Laboratory, Institute of Materials, Ecole Polytechnique Fédérale de Lausanne, Switzerland*
[b]*Phase Solutions Ltd, Lausanne, Switzerland*
[c]*Instituto de Ciencia de Materiales de Aragón, CSIC, Universidad de Zaragoza, Spain*
[d]*Department of Radiology, University Hospital (CHUV), University of Lausanne (UNIL), Switzerland. E-mail: Marijana.Mionic-Ebersold@chuv.ch*
[e]*Center of Biomedical Imaging (CIBM), Lausanne, Switzerland*

† Electronic supplementary information (ESI) available. See DOI: 10.1039/c7ra00687j

‡ Current affiliation of Alla Arakcheeva is: Laboratory of Physics of Complex Matter, Ecole Polytechnique Fédérale de Lausanne (EPFL), CH-1015 Lausanne, Switzerland.

was calculated to correspond to an IONP diameter of ~19 nm for an applied frequency of 300 kHz and magnetic field strengths of 2500–9000 A m^{-1}.[15,23] Unfortunately, using co-precipitation (CP), the most common method to synthesize IONPs, the control over their size and size distribution is thermodynamically limited.[24] In the other frequently used synthesis method, the hydrothermal method (HT), the size control can be achieved by the choice of the synthesis parameters, such as the choice of organic solvent(s) and/or surface-capping agent(s), high temperature and/or pressure.[25] Indeed, regardless of the synthesis route, these parameters are used to control all MNPs' variables important for SAR (shape, magnetic volume, structural order and magnetic properties). However, these synthesis parameters, along with frequently used toxic molecules/ions, are often noncompliant with regulations in nanomedicine,[26] thus impairing clinical translation of numerous reported MNPs with properties showing great potential. For instance, among natural products magnetosomes obtained from AMB-1 magnetotactic bacteria have the highest reported SAR for ferrimagnetic IONPs of 875 W g_{Fe}^{-1} (obtained at 183 kHz and 32 kA m^{-1}, $f{\cdot}H = 5.86 \times 10^9$ A m^{-1} s^{-1}).[27] Among numerous other previous studies, the highest SAR of 509 W g_{Fe}^{-1} for engineered IONPs in the clinical limit (at $f{\cdot}H = 4.8 \times 10^9$ A m^{-1} s^{-1}) has been reported for 19 nm nanocubes synthesized by a non-aqueous thermal decomposition.[28] The highest SAR by microwave-based method was 430 W g_{Fe}^{-1} for citric acid coated multi-core IONPs of 17 nm at 10.5 kA m^{-1} and 950 kHz.[29] On the other side, γ-Fe_2O_3 IONPs synthesized by the aqueous routes such as CP or HT without capping agents typically have SAR values well below 100 W g_{Fe}^{-1} in the clinically relevant conditions.[30,31]

From the above, we identified the goal of developing IONPs with controlled properties to act as efficient mediators for hyperthermia treatment by increased SAR. Further, these IONPs would need to be synthesized in conditions that enable translational research (*e.g.* no toxic molecules/ions, no organic solvent(s), no capping agent(s), minimal elevated temperature and/or pressure). Achieving this goal requires not only detailed understanding of structural–properties relationships, but further correlation of these to the synthesis mechanism in order that the important IONP variables can be controlled.

Here, we report a study of the structure–properties relation in IONPs synthesized by our novel aqueous synthesis route which combines CP and HT treatment, termed CP + HT. This led to IONPs with an optimal set of properties including shape, size (volume), structural order, crystallinity, and saturation magnetization, as well as favourable chemical composition and single domain IONPs. Consequently, our IONPs obtained by the novel aqueous synthesis route CP + HT have increased SAR values as compared to IONPs obtained by CP. Moreover, these results were obtained under conditions facilitating clinical translation, and thus have real potential for the hyperthermia treatment.

Experimental

Synthesis of IONPs

CP synthesis. IONPs were prepared by modified previously established alkaline CP synthesis of ferric and ferrous chlorides in aqueous solution at room temperature.[32,33] Briefly, solutions of $FeCl_3 \cdot 6H_2O$ and $FeCl_2 \cdot 4H_2O$ (the relative fraction of Fe(II) in total Fe amount (R = Fe(II)/[Fe(II) + Fe(III)]) of 0.5) were mixed and precipitated with concentrated ammonia while stirring vigorously. The resulting black precipitate was washed from ammonia several times with ddH_2O until pH decreased to about 7.5. The solid was collected and refluxed in a mixture of 25.7 ml of 0.35 M $Fe(NO_3)_3$ and 17.4 ml of 2 M HNO_3 for 30 min while the initial black slurry turned brown. The system was allowed to cool down to room temperature, the remaining liquid was discarded, and 100 ml of ddH_2O was added to the slurry, which was immediately dispersed. The suspension was washed with ddH_2O and dialyzed (Spectra/Por®; 12–14 kDa) against 10 mM HNO_3 for 48 h by changing the dialysis solution every 10–12 h, and finally, the obtained stable suspensions were stored at 4 °C.

CP + HT synthesis. IONPs were synthesised by our novel CP + HT method with previously optimised synthesis parameters.[34] Briefly, aqueous solutions of $FeCl_3 \cdot 6H_2O$ and $FeCl_2 \cdot 4H_2O$ were prepared at room temperature with the relative fraction of Fe(II) in total Fe amount (R) of 0.5. Afterwards, 6 M ammonia solution was mixed instantaneously with the solution of iron salts under vigorous stirring resulting in the immediate CP process. Note that this CP step was not performed under inert atmosphere, and thus, fast mixing without air bubbles was essential in order to avoid oxidation of iron(II) before co-precipitation happens. The obtained suspension was instantaneously transferred into a sealed autoclave for the HT treatment (without stirring, since the agitation during aging broadens the size distribution)[35] at 120 °C for 24 h. The resulting particles were washed from ammonia several times with ddH_2O until pH 7.5, centrifuged (Beckman Coulter; Avanti J-26 XP; 5 min, 5000 RCF) in order to remove any possible remaining molecules of ammonia and resuspended in 25.7 ml of 0.35 M $Fe(NO_3)_3$ and 17.4 ml of 2 M HNO_3 for oxidation in an oil bath at 120 °C for 30 min. The system was allowed to cool to room temperature, the remaining liquid was discarded, and 100 ml of ddH_2O was added to the slurry, which was immediately dispersed. The suspension was washed with ddH_2O and dialyzed (Spectra/Por®; 12–14 kDa) against 10 mM HNO_3 for 48 h by changing the dialysis solution every 10–12 h, and finally, the obtained stable suspensions were stored at 4 °C.

Characterisation of IONPs

Powder XRD experiment. The experimental powder XRD data were obtained in Swiss-Norwegian beamline (ESRF, Grenoble). The powder sample was taken as supplied and inserted into 0.5 mm diameter, thin-walled glass capillaries. The diffraction patterns were recorded using an incident X-ray beam cross section of 0.3 mm × 0.3 mm. Diffraction patterns have been collected at room temperature. The wavelength λ = 0.6934 Å was selected using the double-crystal monochromator. Powder diffraction was measured using the PILATUS-2M pixel detector. The area detector image was integrated to produce a one-dimensional powder pattern, showing the diffracted intensity as a function of the scattering angle 2θ. A pattern from a reference sample of LaB_6 (lanthanum hexaboride) was collected immediately before the experiment in order to precisely calibrate the sample-to-detector

distance, the beam centre on the detector, and other parameters such as detector tilt. The experimental lattice parameter of the LaB_6 cubic unit cell, $a = 4.15496(4)$ Å, has been measured as equal to published one, $a = 4.1549(1)$ Å (ICSD collection code 152466[36]). JANA2006 program package[37] was used for Rietveld structure refinement and all other structure calculations. The Pseudo-Voigt function combining with the tensor method for the strain broadening was applied for the profile approximation. Legendre polynomials were used for fit of background. Quality of the refinement was checked with examination of the residual electron density, $\Delta\rho$, maps. For the average crystallite size (D) estimation, the measured characteristics, full wide at half maximum, FWHM $= B_{obs}$ and θ angle, along with instrument effect, $B_{std} = 0.05$ for the used device, shape factor $K = 0.9$ and the wavelength $\lambda = 0.6934$ were used in the Scherrer equation:

$$D = K\lambda/[(\pi/180)(B_{obs}{}^2 - B_{std}{}^2)^{1/2}\cos\theta]$$

The contribution of the lattice strain into the line broadening is only 0.5–1.6% B_{obs} in the analysed sample. This contribution affects the average size value beyond the estimation accuracy. The log-normal distribution function has been used for the estimation of the crystallite size distribution:

$$F(x) = [1/(x\sigma\sqrt{2\pi})]\exp\{-[\ln(x/m)]^2/2\sigma^2\}$$

where $m = D$ has been used as an approximation of the median crystallite size; and σ has been taken from the profile fit of each single experimental reflection taken after subtraction of background and correction for the strain effect.

Magnetic characterization. AC susceptibility measurements at 100, 464, 2154 and 10 000 Hz have been performed as a function of temperature, and AC susceptibility measurements at 300 K have been performed as a function of frequency in a PPMS 9T equipment from Quantum Design. $M(H)$ hysteresis cycles were measured in a MPMS 5S equipment also from Quantum Design. The magnetic measurements were carried out in double gelatin capsules loaded with 100 μl of the as prepared sample suspensions. The diamagnetic contribution of the container and the water was also measured and subtracted from the total magnetization.

Hyperthermia measurements. SAR values of 1 ml of IONPs' suspensions at 5 mg_{Fe} ml^{-1} were measured with a magneTherm™ instrument (nanoTherics). In order to generate different field and frequencies, SAR values were measured with the 9 coil turn coupled to the following capacitor array: A200 (177.6 kHz, 23.6 mT), A88 (266.2 kHz, 23.5 mT) and B22 (533.7 kHz, 24.6 kHz). The temperature of the sample was measured with a GaAs fiber optic temperature sensor (OptoCon), inserted in the IONPs' suspension and connected to a fiber optic temperature monitoring system. When the temperature of the sample was stable, the temperature was recorded: (i) 30 s with the field off, (ii) 120 s with the field on and (iii) 30 s with the field off. SAR values (in W $g_{Fe_2O_3}{}^{-1}$) were calculated from the $T(t)$ curves as followed:

$$\mathrm{SAR} = \frac{C_p}{m_{Fe_2O_3}}\frac{\Delta T}{\Delta t}$$

where C_p is the effective specific heat capacity ($(C_{p(H_2O)} \times m_{H_2O}/m_{tot}) + (C_{p(Fe_2O_3)} \times m_{Fe_2O_3}/m_{tot})$), m_{tot} the total mass of the sample, $m_{Fe_2O_3}$ the mass of magnetic material in the sample and $\Delta T/\Delta t$ the slope of the linear part of the heating curve. SAR values are given as the mean of three measurements.

***In vitro* toxicity study.** To determine the cell viability, the colorimetric MTS and PrestoBlue assays were used. HeLa (20000 cells per well) and LnCaP (40000 cells per well) cells were cultured in 96-well plates at 37 °C, and exposed to different concentrations of IONPs (20, 40, 60, 80, 100 and 200 μg_{Fe} ml^{-1}) for 24 h. Cells treated only with medium served as negative controls. After 24 h incubation, the supernatant of each well were removed, cells were washed twice with PBS. For MTS assays, 100 μl of MTS solution (CellTiter 96® AQueous One Solution Cell Proliferation Assay from Promega, diluted 6 times in medium) was added to the cells. After 2 h incubation, the absorbance of the formazan product was measured with a microplate reader (Tecan Infinite M200) at a wavelength of 490 nm. For PrestoBlue assays, 100 μl of PrestoBlue® Cell Viability Reagent (ThermoFisher Scientific, diluted 10 times in medium) was added to the cells. After 1 h incubation, the fluorescence of the resazurin product was measured with a microplate reader (Tecan Infinite M200) at an excitation wavelength of 535 nm and an emission wavelength of 615 nm. All experiments were performed in triplicates. Results are given as means (with standard deviations) of the values obtained in these triplicates. All kinds of cell line, LnCaP and HeLa cells, which were used for this experiment, were purchased from ATCC (ATCC CRL-1740 and ATCC CCL-2, respectively).

Results and discussion

IONPs were synthesized by our novel aqueous synthesis method which combines standard CP and HT treatment, and thus named CP + HT.[34] In our previous study, we optimized the synthesis parameters, such as the Fe^{3+}/Fe^{2+} ratio, base concentration, temperature, synthesis duration, that allowed us control over the size, shape and phase of these IONPs.[34] Briefly, stoichiometric amounts of Fe^{2+} and Fe^{3+} salts were co-precipitated in alkaline milieu and subsequently hydrothermally treated for 24 h. Subsequent oxidation yielded preferred γ-Fe_2O_3 IONPs which were then characterized without size separation, corresponding to IONPs' sample CP + HT. In order to assess if IONPs obtained by this novel synthesis route had advantageous properties with respect to IONPs synthesized by standard CP,[32,33] we studied and compared the properties of both types of IONPs, novel CP + HT and standard CP.

Morphology and composition

Representative transmission electron microscopy (TEM) micrographs of IONPs in samples CP and CP + HT are shown in Fig. 1 (a and b, respectively). The difference in the shape of IONPs in these samples can be seen. IONPs in sample CP had irregular shapes with a tendency towards spherical one (Fig. 1a

and insert). On the contrary, the IONPs in sample CP + HT had clearly defined and mostly faceted surfaces, and also, defined shapes (typically rectangular or ellipsoidal and spherical). Moreover, as expected, IONPs in sample CP + HT exposed to HT treatment resulted in larger particles. The primary particle diameter or equivalent diameter, often termed "TEM diameter", d_T, was calculated from 1000 manually measured IONPs' Feret diameters from representative TEM micrographs (see the Experimental section for calculation details). Fig. 1c shows a distribution of the obtained d_T. The average d_T were (9.0 ± 2.5) nm and (18.1 ± 4.9) nm for IONPs in samples CP and CP + HT, respectively. Besides d_T, the hydrodynamic diameter, d_H, is also important especially for biomedical applications where IONPs are suspended in liquid. An insert in Fig. 1c shows a number weighted distribution of the obtained d_H. The average d_H measured by dynamic light scattering (DLS) were (16.1 ± 4.5) nm and (30.2 ± 9.1) nm from number weighted distributions of IONPs in samples CP and CP + HT, respectively (and from volume weighted distributions d_H were (22.5 ± 13.9) nm and (40.5 ± 16.5) nm, respectively). The measured d_H of IONPs is consistent with the corresponding d_T, indicating typically up to two IONPs per agglomerate. This means that our non-coated IONPs do not strongly aggregate, a property that is preferable for biomedicine. All values obtained for IONPs in sample CP are consistent with previously reported values.[32,33] Evidently, the change in the synthesis route not only reflects a difference in shape of IONPs, but also brings an expected change in the diameter of IONPs.

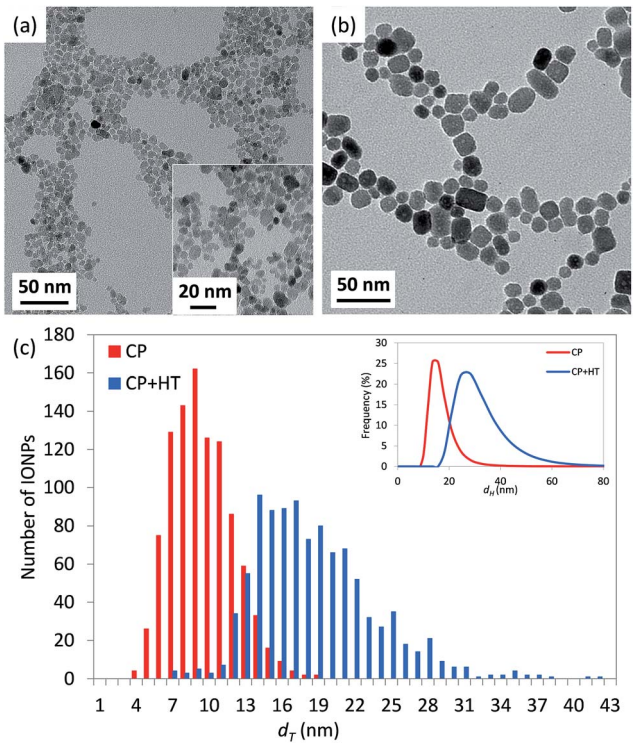

Fig. 1 Representative TEM micrographs of IONPs in samples CP (a) and CP + HT (b). Insert in (a) shows TEM micrograph of the same sample with higher magnification. (c) Shows distribution of the primary particle diameter ("TEM diameter", d_T) and an insert shows a number weighted distribution of the hydrodynamic diameter, d_H, for both samples.

Concerning the composition, infra-red (IR) spectra are often used to discriminate between γ-Fe_2O_3 and Fe_3O_4, since the latter displays one distinct peak at 571 cm^{-1}. In contrast, γ-Fe_2O_3 displays several bands between 800 and 400 cm^{-1} and the number of these bands increases with higher ordering of vacancies.[38,39] The IR spectra of the IONPs both as a suspension and as powders (see Fig. S1a and b†) showed multiple bands between 800 and 400 cm^{-1}, which indicate a structure close to vacancy ordered γ-Fe_2O_3. The structure of the IONPs was also evaluated by X-ray photoelectron spectroscopy (XPS), with the spectra confirming no structural difference between the samples. In addition, the core-level spectra in the Fe 2p regions correspond to γ-Fe_2O_3 [40] (spectra are given in Fig. S2†). Moreover, we have performed UV-vis absorption measurement of IONPs suspensions and the obtained spectra (see Fig. S3†) for samples CP and CP + HT showed a small change in the absorption band maxima (from smaller to larger IONPs' samples, from 227 nm to 232 nm, respectively) with peak broadening for the second sample associated to corresponding diameter broadening. Both, small peak shift and peak broadening were previously observed in transition metal oxides MNPs (especially in a systematic study of UV-vis absorption spectra of MNPs with different shape and size).[41–43]

Structure analysis

Standard powder X-ray diffraction does not allow for distinguishing between different possible γ-Fe_2O_3 structures. Therefore, the structure of IONPs in our samples was studied by the synchrotron radiation powder diffractometry at the Swiss-Norwegian beam-line (ESRF, Grenoble). For the powder XRD pattern of IONPs in sample CP, all diffraction reflections of γ-Fe_2O_3 can be fitted using the magnetite space group $Fd\bar{3}m$ with the cubic unit cell parameter a = 8.3512(2) Å and no superstructure reflections are observed (the powder XRD profiles, experimental, calculated and different, are shown in Fig. S4†); for characteristics of the structural parameters see Table S1.† Refinement of the Fe atom occupation in octahedron (85.5%) and tetrahedron (100%) positions of the magnetite structure leads to the composition $Fe_{2.03(2)}O_3$. Several single diffraction reflections selected for the crystalline diameter estimation (see Table S2†) point to isotropic crystalline diameter with the average value of (9.4 ± 0.1) nm. This value is in agreement with the d_T of (9.0 ± 2.5) nm determined from the TEM study.

On the other side, the structure of IONPs in sample CP + HT turns to be much more complex than in the previous case of CP sample. In fact, the obtained powder XRD pattern of the former sample (Fig. 2) shows one phase – maghemite, γ-Fe_2O_3, and the majority of the diffraction maxima can be fitted using the magnetite space group $Fd\bar{3}m$ with the cubic unit cell parameter a = 8.3551(3) Å. However, three weak reflections, 101, 102 and 112, (marked red in Fig. 2) violate the glide planes d. Hence, the cubic subgroup $P4_332$, which is non-centrosymmetric and free of the d-planes, has been used for the deeper structure

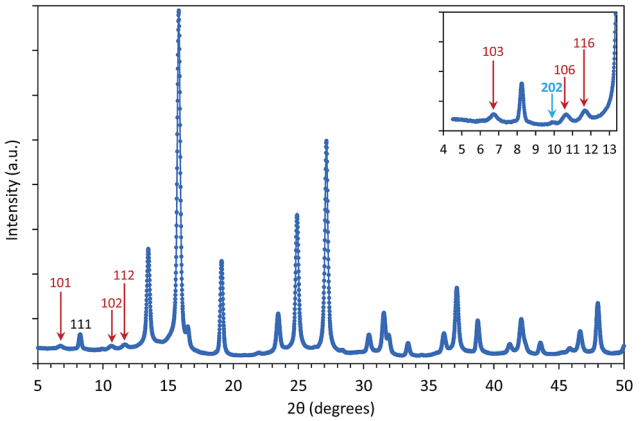

Fig. 2 The powder XRD profile of IONPs in sample CP + HT. Profile fit in space group $P4_332$ with the unit cell parameter $a = 8.3552(4)$ Å. The reflection incompatible with the space group $Fd\bar{3}m$ are indicated by red arrows. In insert, reflections are indexed in tetragonal unit cell with the triple c-parameter: $a_{tet} = a_{cub}$ and $c_{tet} = 3c_{cub}$. Blue arrow points to diffuse reflection 202.

investigation. This space group allows distinguishing between Fe-octahedral positions, being of 62% and 95% occupancy (octa-positions 4b and 12d, respectively), while the tetrahedron position shows of 98.5% occupancy (see a scheme of regular structure in section normal to [1−10] given in Fig. S5a†). The composition has been refined as $Fe_{2.06(2)}O_3$. For this model (Model I in Fig. S5†), residual electron density map (REDM) calculated in the vicinity of Fe and O atoms contains a set of regularly distributed significant extra maxima, which are not associated with the regular structure (Fig. S5b† left panel). The extra maxima have been interpreted as a contribution of enantiomorphous distribution of Fe atoms linked by the inversion centre with the main structure at the same close packing of O atoms (Fig. S5b† right panel). An inclusion of 2% enantiomorphic contribution (Model II in Fig. S5†) removes the extra-maxima from REDM (Fig. S5b† right panel) and better fits the powder XRD profile (experimental, calculated and different are given in Fig. S6†). Characteristics of the structural parameters are given in Table S3.† Some domains of maghemite contain areas with a statistical distribution of Fe atoms corresponding either to the main or to the enantiomorphic modifications. The close packing of O-atoms is homogeneous in each domain, *i.e.* common for both Fe distributions. In average, about 2% Fe atoms match their enantiomorphous distribution. A few possible intergrowth schemes are proposed and shown in Fig. S7.† Interestingly, one very weak diffuse reflection points to a tendency to form a superstructure. This reflection can be indexed as 202 in the tetragonal unit cell with $a_{tet} = a_{cub}$ and $c_{tet} = 3c_{cub}$ (insert in Fig. 2). The average crystallite diameter was estimated equal to (17.4 ± 0.1) nm with practically isotropic variation from 16.6 nm to 18.5 nm depending on the crystallographic direction (see Table S8†). These values are in agreement with the d_T of (18.1 ± 4.9) nm determined by TEM.

The iron vacancies distribution in the octahedral sites in γ-Fe_2O_3, and their degree of ordering have been the focus of studies over several decades.[44–46] In the case that cation vacancies are randomly distributed over the octahedral sites, the space group is $Fd\bar{3}m$ as in magnetite, Fe_3O_4.[12] However, if the iron vacancies are not distributed over all 16 octahedral sites and instead are constrained only to Wyckoff 4b sites, the symmetry in such γ-Fe_2O_3 is $P4_332$.[46] That was firstly proposed by Braun[44] based on the extra reflections in the powder diffraction pattern, as we observe in sample CP + HT. Even further, as firstly proposed by Oosterhout and Rooijmans[45] complete ordering of iron atoms would result in a spinel tetragonal superstructure with spinel cubic cell tripled along the c axis, *e.g.* $c = 3a$, as we also observe in our sample CP + HT. Thus, we observe different iron vacancies ordering in IONPs in our samples. In sample CP, iron vacancies are randomly distributed over all octahedral sites and thus, the space group $Fd\bar{3}m$ could be used. This is in agreement with previous studies which reported that very small NPs of γ-Fe_2O_3 do not show vacancy ordering.[12,46,47] On the contrary, for IONPs in sample CP + HT, space group $P4_332$ has been found implying iron vacancies ordering even with a tendency to form superstructure. The same observation was previously reported for IONPs with crystalline diameter larger than 64 nm or 84 nm.[47] This higher order in the structure of IONPs that we found in the second sample can be associated to the novel synthesis route which includes a HT step that allows for crystallisation and hence, equilibration of iron vacancies.

Magnetic properties

For applications of NPs in hyperthermia treatment, it is crucial to control magnetic properties of the materials, and therefore, detailed characterization of magnetic properties was done for IONPs.

From the measurement of magnetisation as a function of magnetic field strength, H ($M(H)$ curves are given in Fig. 3a), (mass) saturation magnetisation, M_s, can be obtained as a plateau where value of M saturates. In our samples CP and CP + HT (Fig. 3a) M_s of IONPs were 65.5 A m^2 $kg_{Fe_2O_3}{}^{-1}$ and 72 A m^2 $kg_{Fe_2O_3}{}^{-1}$, respectively. The obtained M_s values are lower than M_s of bulk γ-Fe_2O_3, 74 A m^2 kg^{-1}.[48] This is often explained by the existence of a magnetically inactive (also called "dead") layer[49] which consists of disordered spins at the surface of MNPs, as introduced by Sato *et al.*[50] This layer reduces the magnetic volume with respect to the total volume, and the M_s value of the IONPs is lower than that of the bulk, M_{sb}. Thus, M_s measured for MNPs can be written as:[51]

$$M_s = M_{sb}\left(\frac{r-t}{r}\right)^3, \quad (1)$$

where r is the average radius of NPs, t is the thickness of magnetically dead layer, M_s is the saturation magnetisation of IONPs, and M_{sb} is the saturation magnetisation of the bulk γ-Fe_2O_3. Taking into account the value of M_{sb} as 74 A m^2 kg^{-1},[48] from the measured M_s was estimated the thickness of the magnetic dead layer, t, to be 1.8 Å and 0.8 Å, or approximately the length of two and one unit cells for the samples CP and CP + HT, respectively. By taking that into account and approximating IONPs as spheres, the average magnetic volume, V_m, of IONPs in

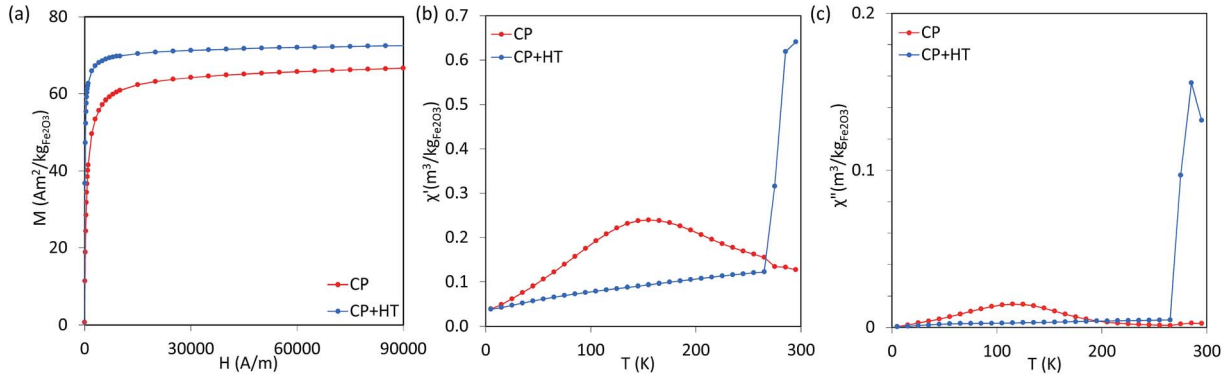

Fig. 3 (a) Magnetization measured as a function of magnetic field strength, H, ($M(H)$ curves) used for extrapolation of saturation magnetisation, M_s. The in-phase (b) and out-of-phase (c) AC susceptibility measurements of suspension of IONPs in both samples as a function of temperature at frequencies of 2154 Hz.

samples CP and CP + HT were 340 nm^3 and 3027 nm^3, respectively. Consequently, the magnetic moment at room temperature were 11 819μ_B and 115 672μ_B for CP and CP + HT IONPs, respectively, calculated by standard equation: $\mu = M_s \rho V_m$, where ρ is the density of γ-Fe_2O_3 (5242 kg m^{-3}).[52] The obtained difference of the order of magnitude is consistent with the difference in the magnetic volume, and with other reported values.[53]

AC susceptibility, χ, *versus* temperature, T, of suspension of IONPs in both samples was measured at a frequency of 2154 Hz (Fig. 3b and c). The obtained curves of both samples showed a gradual increase of χ along with T. The first feature to be outlined is the high jump of the susceptibility when the liquid melts. At this moment the blocked nanoparticles (ferrimagnetic) can rotate following the field in what is called Brownian relaxation. For sample CP a peak can be clearly observed at a T of ~120 K that corresponds to the blocking T, T_B, in a superparamagnetic (SPM) system or to the Verwey transition in a superspin glass (SSG) system.[54] Furthermore, the in-phase (χ') and out-of-phase (χ'') AC susceptibility *versus* T were measured at several frequencies of the alternating field (100 Hz, 464 Hz, 2154 Hz and 10 000 Hz) and the expected peak shift could be observed (Fig. S8 and S9†).

The effective anisotropy constant, K, is often calculated from the blocking temperature T_B, which is for a single domain MNPs given by the expression:[55]

$$T_B = \frac{KV_m}{25k_B}. \quad (2)$$

For relatively small IONPs (roughly with diameter below ~20 nm) T_B can be obtained from DC measurement (a peak in the ZFC curve) or from AC measurement (a peak in the out-of-phase susceptibility, χ'', as a function of temperature).[56] The obtained T_B corresponding to the χ'' peak position is in the range of ~105–125 K (Fig. S8†). This allows us to roughly estimate the effective anisotropy constant K of sample CP from the expression (2), as 10.7–12.7 × 10^4 J m^{-3}. That is in agreement with values of K reported from IONPs of the comparable diameter.[57,58]

For sample CP + HT with average d_T of 18.1 nm (average crystalline diameter 17.4 nm), a peak in χ *vs.* T curve is not visible, as also observed by others that larger IONPs (roughly with diameter above ~20 nm) have T_B above 250–300 K.[59,60] Since such IONPs have T_B above 250 K, meaning above the usual χ *vs.* T measurement range and also above the bifurcation T in ZFC-FC curves, their K has to be obtained by some other mean. In fact, Bean and Livingston[55] derived the following expression for single domain particles in superparamagnetic regime bellow the blocking temperature:

$$H_c = \frac{2K}{M_s}\left[1 - \left(\frac{25k_BT}{KV_m}\right)^{1/2}\right], \quad (3)$$

where K is the effective anisotropy constant, k_B is the Boltzmann constant, V_m is the magnetic volume, T is the temperature, and M_s is the saturation magnetisation. This relation was applied for numerous MNPs.[61,62] IONPs in sample CP + HT having an average diameter of 18.1 nm and a large size distribution, also have T_B above maximal temperature in a frozen state (250 K) used in AC measurement. Therefore, we measured hysteresis curves of IONP suspensions at 250 K, in the frozen state, and at 300 K, in the liquid state, that allowed us to extract the corresponding coercive field H_c and remanent magnetization M_r at both temperatures (see Fig. 4). Sample CP showed the same behaviour at both temperatures, since it is already superparamagnetic at 250 K and therefore it does not show any coercivity either in the frozen or liquid state. The other sample of IONP suspension did not show any significant coercivity at 300 K (see Table S5† for values of H_c and M_r) because even if some individual IONPs in these samples are in the ferrimagnetic state, they are free to rotate in the liquid state. However, by the measurements at 250 K, a temperature below the freezing point, where IONPs cannot rotate, we obtained their real coercivity. For IONPs in sample CP + HT, in $\chi(T)$ curves at all measured frequencies (Fig. S9†) we can observe a kink around ~50 K previously attributed to a relaxation process[39,63] and a kink around ~120 K which is the T of Verwey transition in a SSG system, but also T_B in a SPM system (meaning that former peak could originate from a fraction of small, *e.g.* superparamagnetic,

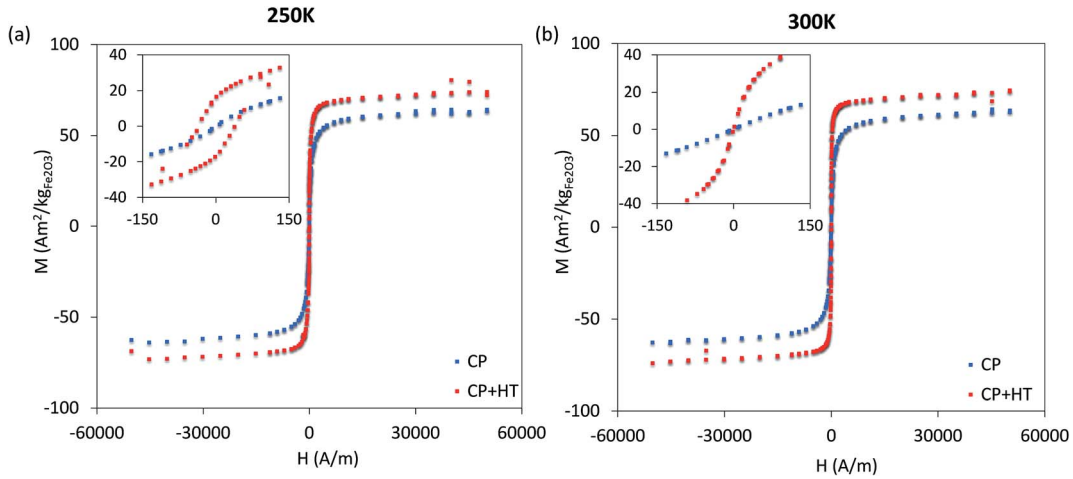

Fig. 4 Hysteresis curves at 250 K in the frozen state and at 300 K in the liquid state, as well as the magnified region around zero for both hysteresis curves (corresponding inserts).

IONPs in sample CP + HT).[54,55,64–66] Both, the χ'' peak position, T_B, in sample CP and kinks in sample CP + HT are strongly frequency dependant as expected in the case of a SPM or a SSG system.[54,66–68] This is in agreement with previous studies of IONPs from almost perfectly non-interacting to interacting conditions (*e.g.* from SPM to SSG system, respectively).[54] In sample CP + HT in frozen state (frozen solvent and thus, fixed positions of IONPs without possibility for Brownian rotation), we could deduce from the hysteresis curve at 250 K (see values for coercivity H_c and remanent magnetization M_r in Table S5†) that M_r/M_s ratio is ~0.2. That clearly shows a system of interacting IONPs even in the frozen state, since M_r/M_s ratio is 0.5 for non-interacting randomly oriented MNPs with uniaxial symmetry.[69] Consequently, the observed fingerprint of SSG behaviour goes along with the system of interacting IONPs in sample CP + HT. Then, we can apply eqn (3) and use the data from the hysteresis curve at 250 K to estimate a K value of 3.1×10^4 J m^{-3} for sample CP + HT.

These values for the effective anisotropy constant of IONPs are in agreement with previously reported values.[57,58,70] We observed an increase of K in the CP sample with smaller diameter of IONPs. This often observed behaviour in small MNPs has been discussed from different contradictory angles. For instance Goya *et al.* attributed enhancement of the MNP's anisotropy mainly to the effect of dipolar interactions.[69] On the other hand, the increase of K in MNPs with smaller diameter is often attributed to the enlarged contribution of surface anisotropy to K. In fact, Bødker *et al.* proposed that K_{eff} has two main contributions, from the volume and the surface anisotropy energy constants, K_v and K_s, respectively.[71] The phenomenological expression which describes this for the spherical MNPs with diameter d is:[71]

$$K = K_v + \frac{6}{d} K_s. \quad (4)$$

In fact, this approach often results in an estimated value of K_v for MNPs close to that of the magnetocrystalline anisotropy energy (first-order) constant of the bulk material.[71] Therefore, we approximated K_v with the magnetocrystalline anisotropy energy (first-order) constant of bulk γ-Fe_2O_3 that is 4.64×10^3 J m^{-3}.[72] Thus, K_s obtained from the expression (4) was 1.69×10^{-4} J m^{-2} for the sample CP which is one order of magnitude higher than K_s of the other sample, 8×10^{-5} J m^{-2}, suggesting a higher contribution of the surface anisotropy to the effective anisotropy for the smaller IONPs, as expected, and reported by others.[71]

Hyperthermia effect

For MNPs, heat dissipation depends on three material's properties: Néel and Brownian relaxation times (related to spin and particle relaxation, respectively), and hysteresis losses. SAR, as a rate of heat dissipation per unit mass of MNPs, is typically determined by these mechanisms. The highest SAR values give MNPs which are ferro/ferrimagnetic and hard magnetic phase.[8,10,15] In spite of this, for nanomedicine are preferred superparamagnetic and soft magnetic phase MNPs, as shown for our IONPs (see Fig. 4 for $M(H)$ curves, and Table S5† for coercivity and remanence). Using the above mentioned values for K leads to a Néel relaxation time of 3.3×10^{-5} s and a Brownian relaxation time of 1.01×10^{-6} s for sample CP; whereas for sample CP + HT relaxation times of 3.79 s (Néel) and 3.91×10^{-6} s (Brownian) were calculated. Thus, for our superparamagnetic IONPs' suspensions, the prevalent relaxation mechanism is the Brownian relaxation with a small contribution of the Néel relaxation, as expected for suspensions.[73]

In order to obtain SAR values, suspensions of IONPs were exposed to AC magnetic field and the increase in temperature with time (heating curve) was measured (Fig. 5a and b). It is worth noting that there are no standards for equipment and measurement procedures of SAR, leading to variability and issues of reproducibility in reported SAR values.[74,75] Thus, the heating curves of all samples were measured minimum three times and the results show less than 10% deviation in-between the measurements (see Fig. S10†). The SAR values were

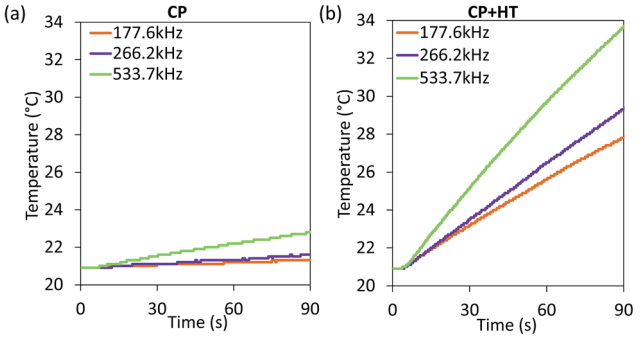

Fig. 5 Heating curves of IONPs in sample CP (a) and CP + HT (b) in aqueous suspension subjected to an AC field (24 kA m^{-1} and three indicated frequencies).

extrapolated from the heating curves (Fig. 5a and b) by using the formula:

$$\mathrm{SAR} = \left(\frac{C_{\mathrm{pH_2O}}}{m_{\mathrm{Fe_2O_3}}}\right)\cdot\left(\frac{\Delta T}{\Delta t}\right), \quad (5)$$

where $m_{\mathrm{Fe_2O_3}}$ is the concentration of IONPs (in gram of γ-Fe_2O_3 per litre), $C_{\mathrm{pH_2O}}$ is the specific heat capacity of water, and $\Delta T/\Delta t$ is the slope of the linear part of the heating curve.

Since SAR depends on parameters of the alternating magnetic field, f and H, SAR values were measured at H of ~24 kA m^{-1} at three different frequencies (177.6 kHz, 266.2 kHz and 533.7 kHz) (Fig. 6a). As expected, SAR increased with increasing frequency, an increase that is more pronounced for larger IONPs, as also observed by others.[76] Besides the correlation of SAR with f and H individually, their product $f{\cdot}H$ is important for clinical applications. As mentioned above, the product $f{\cdot}H$ should be below $\sim 5 \times 10^9$ A m^{-1} s^{-1} for a safe clinical treatment by hyperthermia (this value depends on the exposed volume).[15] Thus, Fig. 6b shows SAR *versus* the $f{\cdot}H$ product and we can see that the highest obtained SAR values at clinically relevant conditions ($f{\cdot}H \leq 5 \times 10^9$ A m^{-1} s^{-1}) are 4.6 W $g_{\mathrm{Fe_2O_3}}^{-1}$ and 57.1 W $g_{\mathrm{Fe_2O_3}}^{-1}$ (6.6 W g_{Fe}^{-1} and 81.6 W g_{Fe}^{-1}) for CP and CP + HT, respectively. This value for sample CP + HT is higher than SAR of 12.5 W $g_{\mathrm{Fe_2O_3}}^{-1}$ reported for IONPs of comparable size (d_T 24.0 ± 5.8 nm) synthesized by the HT route at the same temperature and for the same duration of HT treatment as our sample. Outside of the clinical constrain for the $f{\cdot}H$ product, the highest SAR of 85.7 W $g_{\mathrm{Fe_2O_3}}^{-1}$ (122.5 W g_{Fe}^{-1}) was obtained for sample CP + HT at 533.7 kHz and 24.6 kA m^{-1} ($f{\cdot}H = 10.4 \times 10^9$ A m^{-1} s^{-1}). Moreover, at all frequencies higher SAR values were obtained for samples CP + HT. This was expected based firstly on high crystalline ordering and consequential better magnetic properties than found in the sample with lower SAR, but also based on a relatively broad size distribution of this sample (see Fig. 1c, no size exclusion performed), since smaller and larger IONPs contribute simultaneously to SAR increase by Néel and Brownian relaxations, respectively.[15]

The strong dependence of SAR on f and H makes it difficult to compare SAR values measured at different fields. In order to overcome this issue, intrinsic loss power (ILP) was introduced as SAR normalized to $f{\cdot}H^2$,[77] derived from relaxation theory; it

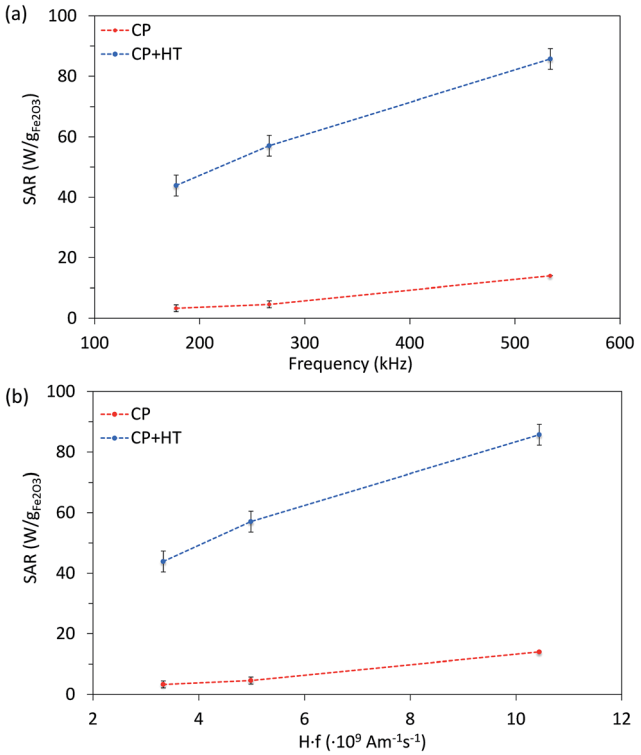

Fig. 6 SAR of both IONP samples as function of frequency at 24 kA m^{-1} (a) and of the $f{\cdot}H$ product (b). Dashed lines are guide for the eyes.

applies only to small field amplitudes and small MNP size (the Néel relaxation model).[15] The ILP values as a function of the $f{\cdot}H$ product for all measured fields and frequencies are given in Fig. 7. The highest obtained ILP value was 0.7 nH m^2 kg^{-1} (SAR = 43.9 W $g_{\mathrm{Fe_2O_3}}^{-1}$, $f{\cdot}H = 3.3 \times 10^9$ A m^{-1} s^{-1}) for sample CP + HT. However, it is clear that for our IONPs the approach of describing heating efficacy by ILP values is incorrect, because the validity of ILP is limited to small field amplitudes and to the Néel relaxation model, which is often neglected, as stressed by Dutz and Hergt.[15] Thus, this approach is applicable for a limited number of systems and is not sufficient to describe the actual heating capability of MNPs.

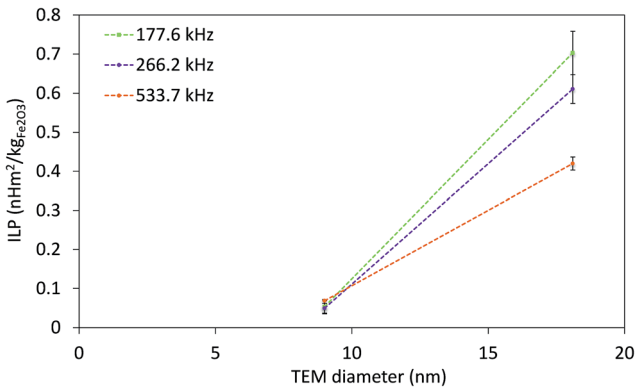

Fig. 7 ILP at three indicated frequencies of both IONP samples as function of TEM diameter. Dashed lines are guide for the eyes.

It has to be pointed out that modelling of SAR does not fit our experimental data suggesting that better understanding of a relation between models and the experimental results is urgently needed. Thus, a consideration of this issue is our next step.

Toxicity

For biomedical applications, it is essential that MNPs are nontoxic. Thus, for a preliminary toxicity assessment, we measured the cell viability (a relative number of live cells incubated 24 h with and without IONPs). The viability of HeLa cells after their exposure to different IONPs' concentrations was assessed with the MTS assay, which measures the intracellular mitochondrial activity *via* the absorbance of the coloured formazan product at 490 nm (Fig. 8a). After 24 h incubation of cells with IONPs, the cell viability was higher than 96% for Fe concentrations up to 200 μg_{Fe} ml^{-1} for both samples. This would suggest that our IONPs are nontoxic. However, it is known that for NPs, different toxicity tests give often different results and thus, lot of effort is placed in standardization and regulations in this domain.[78] Therefore, we also measured the cytotoxicity of IONPs using the PrestoBlue® assay (Fig. 8b), which was obtained from the fluorescence of the resazurin product at 615 nm. The results given in Fig. 6b showed that IONPs in sample CP + HT are nontoxic even for higher concentrations of iron (up to 200 μg_{Fe} ml^{-1}), while IONPs in sample CP showed low toxicity, *e.g.* the viability of HeLa cells was higher than 64% for high iron concentration, 200 μg_{Fe} ml^{-1}. It is known that different cell lines can show different toxicity responses for the same NPs. Since IONPs in sample CP showed low toxicity with HeLa cells, we additionally tested their toxicity with one more cell line (lymph node metastatic cells from prostate cancer, LnCaP cells) by both previously mentioned assays, the MTS assay (Fig. 8c) and the PrestoBlue® assay (Fig. 8d). By the MTS assay (Fig. 8c), we obtained that IONPs of sample CP are nontoxic for both cell lines, while the PrestoBlue® assay (Fig. 6d) showed low and moderate cytotoxicity for higher iron concentration in the case of HeLa and LnCaP cells, respectively. These persistently observed differences in the two assays, the MTS and the PrestoBlue® assays, suggest that there is an urgent need for standardization in the domain of NPs' toxicity assessment and moreover, that better understanding of the MTS method itself is needed. The study in that direction is ongoing.[78,79]

The advantage of CP + HT synthesis

As all previous characterisations showed, compared to sample CP, IONPs in sample CP + HT had advantageous properties arising from high structural order. In fact, all these properties, such as crystalline order, M_s, V_m, t, K, SAR, are mutually

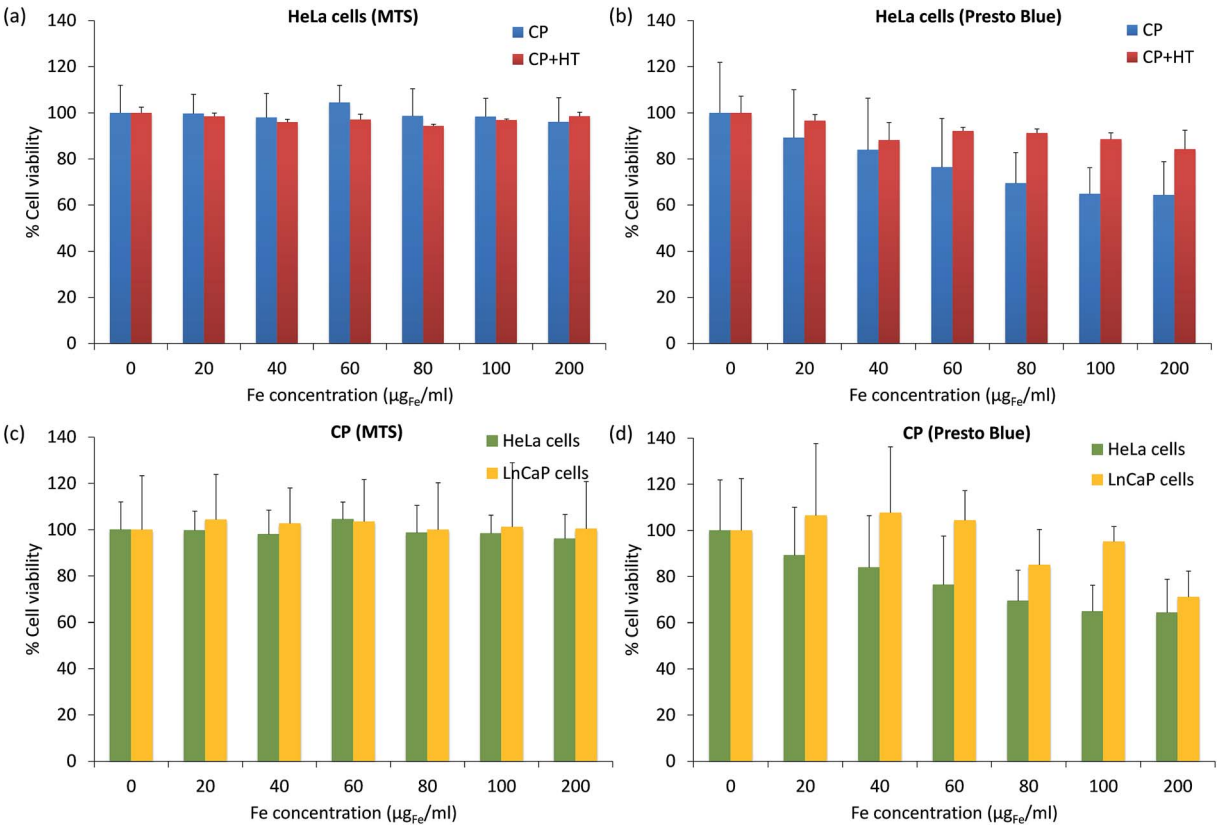

Fig. 8 Cell viability upon exposure to different IONPs' concentrations (Fe concentration was from 0 to 200 μg_{Fe} ml^{-1}) of: HeLa cells assessed by the MTS assay (a) and the PrestoBlue® assay (b) for both samples; HeLa and LnCaP cells assessed by the MTS assay (c) and the PrestoBlue® assay (d) for sample CP.

correlated and "driven" by ordering in the structure. In fact, it has been even reported that vacancy ordering cannot occur in very small IONPs because of numerous reasons, such as: often too short synthesis time and/or too low synthesis temperature, which both do not allow complete development of ordering; but also surface effects which change the preferential distribution of cations and contribute to vacancy disorder.[12,46,47,80] Indeed, iron vacancies ordering has been very rarely reported for small IONPs of ~10 to 30 nm.[51,80] Moreover, these rare results were obtained only for heat treated dry powders. But unfortunately, for biomedical applications IONPs need to remain in suspension. Thus, the challenge of synthesising highly-structurally-ordered IONPs for biomedical applications by solely wet chemistry (without any drying step) was overcome in this work.

As mentioned above, we found in IONPs of sample CP + HT $P4_332$ symmetry with a tendency of iron vacancies ordering to form superstructure. The same observation was previously reported in IONPs with crystalline diameter larger than 64 nm or 84 nm where former IONPs were heat treated for 6 h at 280 °C.[47,81] Here, we obtained highly ordered structure in our IONPs with crystalline diameter of only 17.4 nm as a consequence of the novel synthesis route CP + HT. Thus, under the conditions of our CP + HT synthesis route, previously unexpected vacancy ordering occurs due to the specific synthesis conditions which include a relatively long HT treatment of 24 h at a relatively low temperature of 120 °C that all allow for equilibration of the iron oxide structure.

Moreover, an increase in magnetic properties is coupled with a decrease in spin canting at surface and/or in the bulk on MNP. In fact, it has been shown that among these two effects, the former has lower contribution to diminishing of magnetic properties. Thus, a control over spin canting which result from both structural disorders in the interior and on the surface of IONP is a key factor to control magnetic properties of MNPs, which is the case in our IONPs in sample CP + HT.

Conclusions

In summary, we have studied how our novel synthesis route CP + HT impacts the overall properties of the obtained IONPs and compared these with the corresponding properties of IONPs synthesized by the standard CP method. The results showed that the novel CP + HT synthesis has a strong impact on the overall properties of the obtained IONPs, especially on the magnetic properties and the magnetic heating power of the samples, and yields IONPs with superior properties as compared to IONPs obtained by CP. More importantly, concerning the structure, IONPs obtained by the CP + HT method had $P4_332$ symmetry with a tendency of iron vacancies ordering to form superstructure. Thus, this is the first report of such high structural order in the IONPs synthesised without drying and in addition, with such a small diameter. The higher order in the structure of IONPs in CP + HT sample can be associated to the novel synthesis route which includes a HT step that allows for crystallisation and hence, equilibration of iron vacancies. We also showed that our IONPs synthesized by the CP + HT method are nontoxic. Moreover, the CP + HT synthesis route fulfils requirements of nano-safety regulations. For all these reasons, the reported IONPs have real potential for biomedical applications.

Acknowledgements

This work was financially supported by the MagnetoTeranostics project that was scientifically evaluated by the Swiss National Science Foundation (SNSF), financed by the Swiss Confederation and funded by Nano-Tera.ch (Magnetotheranostics project No 530 627) and by the Nanoneck2 project funded by Eurostars (Project E!9309 Nanoneck2). We thank to the Interdisciplinary Centre for Electron Microscopy (CIME), Central Environmental Laboratory (CEL) and the Molecular and Hybrid Materials Characterisation Center (MHMC) all at EPFL for access to their facilities and technical support. We are also grateful to Phil Pattison and Swiss-Norwegian beamline (ESRF, Grenoble) for the synchrotron radiation XRD experiments. This work was partially supported by the Spanish Ministry of Science and Innovation (MAT2014-54975-R). The authors would like to acknowledge the use of Servicio General de Apoyo a la Investigación-SAI, Universidad de Zaragoza.

References

1 S. Singamaneni, V. N. Bliznyuk, C. Binek and E. Y. Tsymbal, *J. Mater. Chem.*, 2011, **21**, 16819–16845.
2 T. Neuberger, B. Schöpf, H. Hofmann, M. Hofmann and B. von Rechenberg, *Proc. Fifth Int. Conf. Sci. Clin. Apllications Magn. Carr.*, 2005, vol. 293, pp. 483–496.
3 R. Piñol, C. D. S. Brites, R. Bustamante, A. Martínez, N. J. O. Silva, J. L. Murillo, R. Cases, J. Carrey, C. Estepa, C. Sosa, F. Palacio, L. D. Carlos and A. Millán, *ACS Nano*, 2015, **9**, 3134–3142.
4 T. Hoare, B. P. Timko, J. Santamaria, G. F. Goya, S. Irusta, S. Lau, C. F. Stefanescu, D. Lin, R. Langer and D. S. Kohane, *Nano Lett.*, 2011, **11**, 1395–1400.
5 C. Tassa, S. Y. Shaw and R. Weissleder, *Acc. Chem. Res.*, 2011, **44**, 842–852.
6 T. Gillich, C. Acikgöz, L. Isa, A. D. Schlüter, N. D. Spencer and M. Textor, *ACS Nano*, 2013, **7**, 316–329.
7 O. Pascu, E. Carenza, M. Gich, S. Estradé, F. Peiró, G. Herranz and A. Roig, *J. Phys. Chem. C*, 2012, **116**, 15108–15116.
8 S. Noh, W. Na, J. Jang, J.-H. Lee, E. J. Lee, S. H. Moon, Y. Lim, J.-S. Shin and J. Cheon, *Nano Lett.*, 2012, **12**, 3716–3721.
9 V. Mameli, A. Musinu, A. Ardu, G. Ennas, D. Peddis, D. Niznansky, C. Sangregorio, C. Innocenti, N. T. K. Thanh and C. Cannas, *Nanoscale*, 2016, **8**, 10124–10137.
10 J.-H. Lee, J. Jang, J. Choi, S. H. Moon, S. Noh, J. Kim, J.-G. Kim, I.-S. Kim, K. I. Park and J. Cheon, *Nat. Nanotechnol.*, 2011, **6**, 418–422.
11 A. Walter, C. Billotey, A. Garofalo, C. Ulhaq-Bouillet, C. Lefèvre, J. Taleb, S. Laurent, L. Vander Elst, R. N. Muller, L. Lartigue, F. Gazeau, D. Felder-Flesch and S. Begin-Colin, *Chem. Mater.*, 2014, **26**, 5252–5264.

12 R. M. Cornell and U. Schwertmann, *The Iron Oxides: Structure, Properties, Reactions, Occurences and Uses*, Wiley Online Library, Wiley-VCH Verlag GmbH & Co. KGaA, 2nd edn, 2004.
13 T. S. Koskenkorva-Frank, G. Weiss, W. H. Koppenol and S. Burckhardt, *Free Radical Biol. Med.*, 2013, **65**, 1174–1194.
14 A. N. Ilinskaya and M. A. Dobrovolskaia, *Nanomedicine*, 2013, **8**, 969–981.
15 S. Dutz and R. Hergt, *Nanotechnology*, 2014, **25**, 452001.
16 C. J. Busch, in *Verhandlungen des naturhistorischen Vereines der preussischen Rheinlande und Westphalens*, Max Cohen and Sohn, Bonn, ANDRÄ, C.J., 1866.
17 A. Jordan, R. Scholz, P. Wust, H. Fähling and R. Felix, *J. Magn. Magn. Mater.*, 1999, **201**, 413–419.
18 A. Jordan, R. Scholz, K. Maier-Hauff, M. Johannsen, P. Wust, J. Nadobny, H. Schirra, H. Schmidt, S. Deger, S. Loening, W. Lanksch and R. Felix, *Proc. Third Int. Conf. Sci. Clin. Appl. Magn. Carr.*, 2001, vol. 225, pp. 118–126.
19 W. J. Atkinson, I. A. Brezovich and D. P. Chakraborty, *IEEE Trans. Biomed. Eng.*, 1984, **BME-31**, 70–75.
20 R. Hergt and S. Dutz, *Proc. Sixth Int. Conf. Sci. Clin. Appl. Magn. CarriersSCAMC-06*, 2007, vol. 311, pp. 187–192.
21 MagForce AG, 2017.
22 J. Carrey, B. Mehdaoui and M. Respaud, *J. Appl. Phys.*, 2011, **109**, 83921.
23 R. E. Rosensweig, *J. Magn. Magn. Mater.*, 2002, **252**, 370–374.
24 J.-P. Jolivet, C. Chaneac and E. Tronc, *Chem. Commun.*, 2004, 481–483.
25 S. Laurent, D. Forge, M. Port, A. Roch, C. Robic, L. Vander Elst and R. N. Muller, *Chem. Rev.*, 2008, **108**, 2064–2110.
26 M. Hofmann-Amtenbrink, D. W. Grainger and H. Hofmann, *Nanomedicine: Nanotechnology, Biology and Medicine*, 2015, **11**, 1689–1694.
27 E. Alphandéry, S. Faure, O. Seksek, F. Guyot and I. Chebbi, *ACS Nano*, 2011, **5**, 6279–6296.
28 P. Guardia, R. Di Corato, L. Lartigue, C. Wilhelm, A. Espinosa, M. Garcia-Hernandez, F. Gazeau, L. Manna and T. Pellegrino, *ACS Nano*, 2012, **6**, 3080–3091.
29 C. Blanco-Andujar, D. Ortega, P. Southern, Q. A. Pankhurst and N. T. K. Thanh, *Nanoscale*, 2015, **7**, 1768–1775.
30 E. Garaio, J. M. Collantes, J. A. Garcia, F. Plazaola, S. Mornet, F. Couillaud and O. Sandre, *J. Magn. Magn. Mater.*, 2014, **368**, 432–437.
31 S. Gyergyek, D. Makovec, M. Jagodič, M. Drofenik, K. Schenk, O. Jordan, J. Kovač, G. Dražič and H. Hofmann, *J. Alloys Compd.*, 2017, **694**, 261–271.
32 M. Chastellain, A. Petri and H. Hofmann, *J. Colloid Interface Sci.*, 2004, **278**, 353–360.
33 A. Petri-Fink, M. Chastellain, L. Juillerat-Jeanneret, A. Ferrari and H. Hofmann, *Biomaterials*, 2005, **26**, 2685–2694.
34 D. Bonvin, H. Hofmann and M. M. Ebersold, *J. Nanopart. Res.*, 2016, **18**, 376.
35 T. Sugimoto and E. Matijević, *J. Colloid Interface Sci.*, 1980, **74**, 227–243.
36 G. Ning and R. L. Flemming, *J. Appl. Crystallogr.*, 2005, **38**, 757–759.
37 V. Petříček, M. Dušek and L. Palatinus, *Z. Kristallog. – Cryst. Mater.*, 2014, **229**, 345–352.
38 W. Baaziz, B. P. Pichon, S. Fleutot, Y. Liu, C. Lefevre, J.-M. Greneche, M. Toumi, T. Mhiri and S. Begin-Colin, *J. Phys. Chem. C*, 2014, **118**, 3795–3810.
39 T. J. Daou, J. M. Grenèche, G. Pourroy, S. Buathong, A. Derory, C. Ulhaq-Bouillet, B. Donnio, D. Guillon and S. Begin-Colin, *Chem. Mater.*, 2008, **20**, 5869–5875.
40 A. P. Grosvenor, B. A. Kobe, M. C. Biesinger and N. S. McIntyre, *Surf. Interface Anal.*, 2004, **36**, 1564–1574.
41 S. Kundu and M. Jayachandran, *J. Nanopart. Res.*, 2013, **15**, 1543.
42 S. Kundu, M. D. Mukadam, S. M. Yusuf and M. Jayachandran, *CrystEngComm*, 2012, **15**, 482–497.
43 X. He, X. Song, W. Qiao, Z. Li, X. Zhang, S. Yan, W. Zhong and Y. Du, *J. Phys. Chem. C*, 2015, **119**, 9550–9559.
44 P. B. Braun, *Nature*, 1952, **170**, 1123.
45 G. W. Van Oosterhout and C. J. M. Rooijmans, *Nature*, 1958, **181**, 44.
46 R. Grau-Crespo, A. Y. Al-Baitai, I. Saadoune and N. H. D. Leeuw, *J. Phys.: Condens. Matter*, 2010, **22**, 255401.
47 T. J. Bastow, A. Trinchi, M. R. Hill, R. Harris and T. H. Muster, *J. Magn. Magn. Mater.*, 2009, **321**, 2677–2681.
48 C. J. Goss, *Phys. Chem. Miner.*, 1988, **16**, 164–171.
49 A. Millan, A. Urtizberea, N. J. O. Silva, F. Palacio, V. S. Amaral, E. Snoeck and V. Serin, *J. Magn. Magn. Mater.*, 2007, **312**, L5–L9.
50 T. Sato, T. Iijima, M. Seki and N. Inagaki, *J. Magn. Magn. Mater.*, 1987, **65**, 252–256.
51 M. P. Morales, S. Veintemillas-Verdaguer, M. I. Montero, C. J. Serna, A. Roig, L. Casas, B. Martínez and F. Sandiumenge, *Chem. Mater.*, 1999, **11**, 3058–3064.
52 D. Jiles, *Introduction to Magnetism and Magnetic Materials, Third Edition*, CRC Press, Taylor & Francis Group, 2015.
53 B. H. Kim, N. Lee, H. Kim, K. An, Y. I. Park, Y. Choi, K. Shin, Y. Lee, S. G. Kwon, H. B. Na, J.-G. Park, T.-Y. Ahn, Y.-W. Kim, W. K. Moon, S. H. Choi and T. Hyeon, *J. Am. Chem. Soc.*, 2011, **133**, 12624–12631.
54 K. Hiroi, K. Komatsu and T. Sato, *Phys. Rev. B: Condens. Matter Mater. Phys.*, 2011, **83**, 224423.
55 C. P. Bean and J. D. Livingston, *J. Appl. Phys.*, 1959, **30**, S120–S129.
56 D. E. Madsen, M. F. Hansen and S. Mørup, *J. Phys.: Condens. Matter*, 2008, **20**, 345209.
57 M. Chastellain, A. Petri and H. Hofmann, *J. Colloid Interface Sci.*, 2004, **278**(2), 353–360.
58 M. Chastellain, A. Petri, A. Gupta, K. v. Rao and H. Hofmann, *Adv. Eng. Mater.*, 2004, **6**, 235–241.
59 T. Hyeon, S. S. Lee, J. Park, Y. Chung and H. B. Na, *J. Am. Chem. Soc.*, 2001, **123**, 12798–12801.
60 S. Mørup and E. Tronc, *Phys. Rev. Lett.*, 1994, **72**, 3278–3281.
61 F. E. Luborsky and T. O. Paine, *J. Appl. Phys.*, 1960, **31**, S68–S70.
62 D. H. Han, J. P. Wang and H. L. Luo, *J. Magn. Magn. Mater.*, 1994, **136**, 176–182.
63 V. Skumryev, H. J. Blythe, J. Cullen and J. M. D. Coey, *J. Magn. Magn. Mater.*, 1999, **196–197**, 515–517.

64 D. Parker, V. Dupuis, F. Ladieu, J.-P. Bouchaud, E. Dubois, R. Perzynski and E. Vincent, *Phys. Rev. B: Condens. Matter Mater. Phys.*, 2008, **77**, 104428.
65 S. Nakamae, Y. Tahri, C. Thibierge, D. L'Hôte, E. Vincent, V. Dupuis, E. Dubois and R. Perzynski, *J. Appl. Phys.*, 2009, **105**, 07E318.
66 J. A. De Toro, S. S. Lee, D. Salazar, J. L. Cheong, P. S. Normile, P. Muñiz, J. M. Riveiro, M. Hillenkamp, F. Tournus, A. Tamion and P. Nordblad, *Appl. Phys. Lett.*, 2013, **102**, 183104.
67 M. J. Benitez, D. Mishra, P. Szary, G. A. B. Confalonieri, M. Feyen, A. H. Lu, L. Agudo, G. Eggeler, O. Petracic and H. Zabel, *J. Phys.: Condens. Matter*, 2011, **23**, 126003.
68 P. Nordblad, *Phys. Scr.*, 2013, **88**, 58301.
69 G. F. Goya, T. S. Berquó, F. C. Fonseca and M. P. Morales, *J. Appl. Phys.*, 2003, **94**, 3520–3528.
70 L. Lartigue, C. Innocenti, T. Kalaivani, A. Awwad, M. del M. Sanchez Duque, Y. Guari, J. Larionova, C. Guérin, J.-L. G. Montero, V. Barragan-Montero, P. Arosio, A. Lascialfari, D. Gatteschi and C. Sangregorio, *J. Am. Chem. Soc.*, 2011, **133**, 10459–10472.
71 F. Bødker, S. Mørup and S. Linderoth, *Phys. Rev. Lett.*, 1994, **72**, 282–285.
72 C. J. Serna and M. P. Morales, in *Surface and Colloid Science*, ed. E. Matijević and M. Borkovec, Springer US, 2004, pp. 27–81.
73 S. Gyergyek, M. Drofenik and D. Makovec, *Acta Chim. Slov.*, 2014, **61**, 488–496.
74 *COST Multifunct. Nanoparticles Magn. Hyperth. Indirect Radiat. Ther. RADIOMAG*, 2017.
75 B. Sanz, M. P. Calatayud, N. Cassinelli, M. R. Ibarra and G. F. Goya, *Eur. J. Inorg. Chem.*, 2015, **2015**, 4524–4531.
76 P. de la Presa, Y. Luengo, M. Multigner, R. Costo, M. P. Morales, G. Rivero and A. Hernando, *J. Phys. Chem. C*, 2012, **116**, 25602–25610.
77 M. Kallumadil, M. Tada, T. Nakagawa, M. Abe, P. Southern and Q. A. Pankhurst, *Proc. Seventh Int. Conf. Sci. Clin. Appl. Magn. Carr.*, 2009, vol. 321, pp. 1509–1513.
78 *NANoREG*, 2017.
79 *NanoScreen*, 2017.
80 K. Haneda and A. H. Morrish, *Solid State Commun.*, 1977, **22**, 779–782.
81 K. M. Spiers, J. D. Cashion and K. A. Gross, *Key Eng. Mater.*, 2004, **254–256**, 213–216.